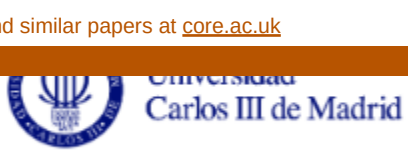

Agüera, N., Cafiero, G., Astarita, T., Discetti, S. (2016). Esemble 3D PTV for high resolution turbulent statistics. *Measurement Science and Technology*, vol. 27, no. 12. DOI: 10.1088/0957-0233/27/12/124011

Ensemble 3D PTV for high resolution turbulent statistics

Nereida Agüera[1], Gioacchino Cafiero[2], Tommaso Astarita[2] & Stefano Discetti[*1]

[1]Aerospace Engineering Group, Universidad Carlos III de Madrid, Avda. de la Universidad 30, 28911 Leganes (Spain)
[2]Department of Industrial Engineering, Universitá degli Studi di Napoli Federico II, P.le Tecchio 80, 80125, Napoli (Italy)

E-mail: [*]sdiscett@ing.uc3m.es

Abstract. A method to extract turbulent statistics from three-dimensional (3D) PIV measurements via ensemble averaging is presented. The proposed technique is a 3D extension of the ensemble particle tracking velocimetry methods, which consist in summing distributions of velocity vectors calculated on low image density samples and then extract the statistical moments from the velocity vectors within sub-volumes, with the size of the sub-volume depending on the desired number of particles and on the available number of snapshots.

The extension to 3D measurements poses the additional difficulty of sparse velocity vectors distributions, thus requiring a large number of snapshots to achieve high resolution measurements with a sufficient degree of accuracy. At the current state, this hinders the achievement of *single-voxel* measurements, unless millions of samples are available. Consequently, one has to give up spatial resolution and live with still relatively large (if compared to the voxel) sub-volumes. This leads to the further problem of the possible occurrence of a residual mean velocity gradient within the sub-volumes, which significantly contaminates the computation of second order moments.

In this work, we propose a method to reduce the residual gradient effect, allowing to reach high resolution even with relatively large interrogation spots, therefore still retrieving a large number of particles on which it is possible to calculate turbulent statistics. The method consists in applying a polynomial fit to the velocity distributions within each sub-volume trying to mimic the residual mean velocity gradient.

Keywords: 3D PTV, Turbulent statistics, Reynolds stresses

This is a post-print version of the paper *Agüera, N., Cafiero, G., Astarita, T., Discetti, S. (2016). Ensemble 3D PTV for high resolution turbulent statistics. Measurement Science and Technology, 27(12), 124011, doi: https://doi.org/10.1088/0957-0233/27/12/124011*

1. Introduction

In the last decades, the inexorable advancement of computer technologies impulsed the development and the extensive application of computational fluid dynamics. Notwithstanding with the great progresses reached in recent years, direct numerical simulation of the Navier-Stokes equations is still limited to relatively low Reynolds number flows (if compared to those of interest for the industry). Consequently, the lead for industrial applications has been maintained by RANS (Reynolds Averaged Navier-Stokes equations) simulations, which need high resolution / high accuracy experimental benchmarks to validate turbulence closure models. For this reason, experimental aerodynamics has been pushed towards its limit with the aim, among others, to provide high resolution 3D statistics on turbulent flows.

Following this line of thought, Tomographic Particle Image Velocimetry (Tomo-PIV, Elsinga et al, 2006) has demonstrated a huge potential since its early stages and it could be considered the most versatile and powerful experimental technique to extract three-dimensional (3D) three-components (3C) velocity field information. Tomo-PIV is based on reconstructing the particles' intensity distribution within an illuminated volume from multiple camera views captured simultaneously. Using the light intensity information along each line of sight as an additional aid to the simple triangulation of Particle Tracking velocimetry (PTV), Tomo-PIV can work with significantly higher image density than PTV (typically $0.05 - 0.10$ ppp, i.e. particles per pixel, instead of the maximum 0.005 ppp affordable by a 4 cameras system in 3D PTV, Maas et al, 1993). Nonetheless, the main weakness of Tomo PIV is its limited spatial resolution. Indeed, the seeding density (and, consequently, the achievable resolution) is limited by the occurrence of ghost particles (Maas et al, 1993) due to the under-determined nature of the tomographic reconstruction problem. Ghost particles are spurious intensity peaks in the reconstructed volume, formed at the intersection of the lines of sight of the different cameras of the system carrying non-zero intensity which pertains to true particles located elsewhere. Ghost particles move according to the average displacement of the set of particles generating them, thus smearing out velocity gradients and reducing the effective spatial resolution (Elsinga et al, 2011).

An estimate of the fraction of ghost particles is given by Discetti and Astarita (2014):

$$\frac{N_{ghost}}{N_{true}} \approx N_{ppp} d_\tau L_z (1 - e^{-N_s})^{N_{cam}-2} \tag{1}$$

where N_{ppp} is the particle image density expressed in particles per pixel, d_τ is the particle image diameter in pixels, L_z is the volume depth, $N_s = N_{ppp}\pi d_\tau^2/4$ is the source density and N_{cam} is the number of cameras. For instance, for the typical case of a volume of $50 \times 50 \times 10\,\mathrm{mm}^3$ discretized with 20 voxels/mm, for an image density of 0.05 ppp, particle image diameter of 2.5 pixels (thus leading to $N_s = 0.24$) and four cameras, the ghost fraction is approximately 120%. Doubling the imaging density leads rapidly to a ghost fraction of more than 700%. Typically, a compromise between the number of

seeding particles and the *ghost/true ratio* has to be achieved. Obviously, maximizing the particle image density N_{ppp} is fundamental to improve the spatial resolution and we can easily relate this magnitude to the size of the interrogation window D_I, supposing N_I particles are sufficient to achieve an acceptable signal to noise ratio:

$$D_I = \sqrt[3]{\frac{N_I L_z}{N_{ppp}}} \tag{2}$$

In this fashion, for the case of 0.05 ppp using the same setup as in the previous example and supposing $N_I = 7$, we are left with an interrogation window size $D_I \approx 30$ voxels (see Discetti (2013) for a more detailed discussion on the effects of the experimental parameters on the window size). The affordable image density can be increased with advanced methods exploiting time coherence in time-resolved experiments (see, for instance, the Sequential Motion Tracking Enhancement by Lynch and Scarano (2015), based on time-marching prediction of the particles' distributions updated with the common algebraic methods for tomographic reconstruction), or in two-frames Tomo-PIV scenario, with techniques based on features-oriented improvement of the reconstructed volume, such as, for example, the Spatial Filtering Improved Tomographic PIV by Discetti et al (2013), which is based on filtering the reconstructed distributions to reduce discretization artifacts and particles elongation. Nevertheless, even by doubling N_{ppp}, according to Eq. 2 the spatial resolution is improved only by a factor of $2^{-1/3}$, i.e. about 20%.

The spatial resolution of turbulent statistics can be improved following an alternative approach rather than increasing the resolution of the instantaneous measurements. Some solutions can be borrowed from the developments in 2D PIV. Single-pixel ensemble correlation (Westerweel et al, 2004), which relies on summing correlation maps to shrink the size of the interrogation window down to a single pixel, is a potential candidate. Its capabilities have been recently extended to the computation of Reynolds stresses (Scharnowski et al, 2012) by extracting the pdf of the velocity fluctuations from the ensemble correlation maps. In the more general scenario of volumetric data provided by either tomographic PIV or holographic PIV, as well as for standard planar PIV, Soria and Willert (2012) presented a method to extract the joint probability density function of turbulent flows from the correlation maps. Moreover, the rate of convergence of ensemble correlation has been recently improved by the use of symmetric double correlation (Avallone et al, 2015), thus reducing by a factor of $\sqrt{2}$ the number of samples needed to achieve a prescribed accuracy and widening the portfolio of applications in planar PIV. However, on one side the spatial resolution of single-pixel ensemble correlation is limited by the particle image diameter (Kähler et al, 2012), which indeed averages out the displacement field on the size of the imaged spot. On the other side, its implementation in 3D tomographic PIV is complex due to the large computational cost and memory requirements.

In this work, we extend to 3D the ensemble particle tracking procedure outlined in Kähler et al (2012) and propose significant improvements which would make the

application of the technique feasible for the extraction of turbulent statistics down to the single voxel or possibly beyond that. For PTV, the spatial resolution is no longer limited by the particle image diameter but by the error in the determination of the position of the particle images corresponding to a particle image pair. The idea is to improve the spectral response of the window on which the vectors are spatially averaged in order to reduce significantly the number of samples required to achieve the desired spatial resolution and accuracy. In Sec.2 the ensemble PTV process and the algorithm for resolution improvement are described. The algorithms are validated with 2D and 3D synthetic test cases in Sec.3, and tested in an experimental scenario in Sec.4.

2. Ensemble Particle Tracking Velocimetry

The Ensemble PTV (EPTV) process is sketched in Figure 1 and conceptually detailed below.

Step 1 - Image acquisition The images are captured simultaneously from different angles, as in the traditional 3D PTV/Tomo-PIV fashion.

Step 2 - Particles identification The particles' position are identified on the images, and then triangulated in space. Sub-pixel precision is achieved by using a combination of 1D Gaussian fits on the particles intensity. The triangulation procedure used in this work is the one outlined in Discetti and Astarita (2014). In order to reduce the number of ghost matchings, a relatively small particle image density should be used, according to Eq. 1. This aspect is discussed in more detail later in this section.

Step 3 - Particle matching Particle pairs should be identified between subsequent exposures. Since the particles' spacing is larger than in planar PIV, the choice of the matching algorithm is less critical. In most cases, a rough velocity predictor obtained by low resolution Tomo-PIV is enough to enable a nearest neighbour search with very high reliability.

Step 4 - Ensemble creation Particle matches coming from the different image pairs are all included into a single ensemble to increase the spatial density of the velocity vectors.

Step 5 - Averaging An interrogation spot size is selected according to the number of samples and the number of particles desired in each spot. In this work, spherical interrogation volumes have been used, whose radius was chosen depending on the ensemble density of velocity vectors. The local statistical moments of the velocity can be extracted from the statistical dispersion of the velocity vectors.

2.1. Choice of the number of samples

The number of samples required to achieve, with the desired spatial resolution, a certain uncertainty on the statistics due to the random fluctuations can be easily obtained by

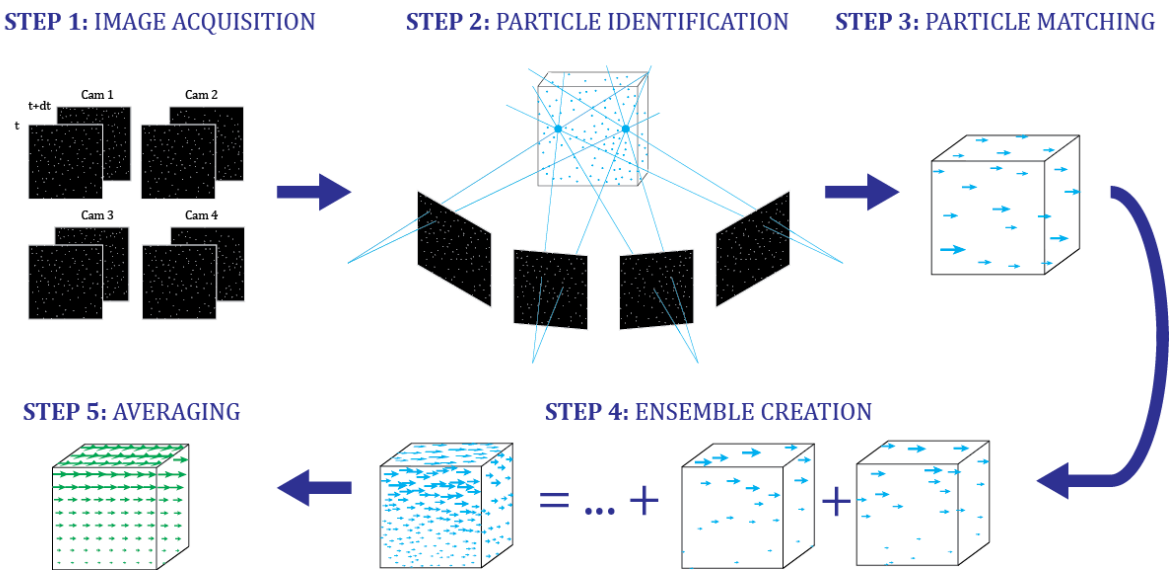

Figure 1: Sketch of the ensemble PTV process.

using the well-known relations for the standard error of the mean and of the variance. For example, the standard error of the mean is given by:

$$\sigma_U = \frac{\sqrt{u'^2 + \sigma^2}}{\sqrt{N_p}} \tag{3}$$

where u' is the standard deviation of the velocity fluctuations and σ is the random error due to the incorrect particles positioning. For example, assuming that $u'^2 >> \sigma^2$ and that 1% accuracy is required on the mean velocity for the case of 10% turbulence intensity, then $N_p = 100$ statistically independent particles are required.
The standard error of the variance can be roughly estimated, under the assumption that $u'^2 >> \sigma^2$ and of Gaussian statistical moments of the turbulent fluctuations, as follows:

$$\sigma_{u'^2} = \frac{\sqrt{2}u'^2}{\sqrt{N_p}} \tag{4}$$

thus leading, for the same example detailed above, to around 800 particles to get 5% accuracy on the turbulent fluctuations.

Then, given a set of N_{snap} snapshots, it turns out that, for a spherical averaging region of diameter D_I:

$$\frac{4}{3}\pi\left(\frac{D_I}{2}\right)^3 \frac{N_{ppp}}{L_z} N_{snap} = N_{part} \tag{5}$$

In the end, the best achievable D_I is set by practical limitations. For instance, from Eq. 5 it comes that, for $D_I = 1$ voxel, $N_{ppp} = 0.01$ ppp, $L_z = 200$ voxels and $N_{part} = 800$ particles, more than 30 million statistically independent samples would be required, which would results in 565 hours of experiment if capturing at $15Hz$. Luckily, just by increasing D_I to 8 voxels, this requirement leads to 60000 samples, which is certainly more affordable.

2.2. Choice of the particle image density

Unless advanced methods are used (see, for instance, the Iterative Particle Reconstruction, Wieneke, 2013) it is desirable to have a relatively small particle image density so that the number of ghost particles is limited and the reconstruction can be performed with a straightforward triangulation. While this might be perceived as moving in the opposite direction to that of reducing the number of samples, as it can be seen in Eq. 1, the ghost fraction increases more than linearly with the particle image density while the interrogation spot size is only linearly dependent on N_{ppp}, as can be extracted from Eq. 5. Indeed, according to Eq. 5, a reduction of a factor of 5 in the particle image density can be easily compensated by increasing the size of D_I by a factor of ~ 1.7, and/or by increasing the number of samples.

There are two additional fundamental reasons to set a low value of the image density:

- The computational cost is consistently reduced if the particles' identification can be performed by straightforward triangulation. This aspect compensates the larger number of samples required to reach the same results as indicated by Eq. 5 when reducing N_{ppp}. Additionally, only particles peaks are of interest, so the image can be stored in sparse format, thus reducing memory storage.
- The principal source of random error in the particles' location is due to the occurrence of overlapping particles. Nobach and Honkanen (2005) documented that 1D Gaussian interpolation along each physical direction locates the particles with an uncertainty ranging between $0.02 - 0.05$ pixels, provided that the particle image diameter is larger than 2.5 pixels, which is the typical situation of 3D PIV experiments, in which a relatively large $f_\#$ is required to achieve proper focusing throughout the depth of the imaged volume. Besides, this uncertainty can be further reduced with 2D regression in the case of elliptical non-axially orientated particles. This is true for isolated particles, while for partially overlapping particles the uncertainty can be as large as 0.5 pixels. Furthermore, this error is transmitted to the estimation of the variance of the velocity vectors, thus contaminating second order moments. According to Adrian (1991), the probability of overlapping particles can be obtained via a Poisson distribution:

$$Pr(0\,\text{particles}) = e^{-N_s} \tag{6}$$

$$Pr(1\,\text{particle}) = N_s e^{-N_s} \tag{7}$$

For instance, for a particle image density of 0.01 ppp, corresponding to a source density of 0.05 for a particle image diameter of 2.5 pixels, the probability of having zero particles overlapping is more than 95%. If the particle image density increases to 0.10 ppp, thus resulting in $N_s = 0.49$, this probability reduces to 61%. Additionally, as argued previously, according to Eq. 1, the ghost particles fraction would be of the order of around 750% for a 4 cameras system.

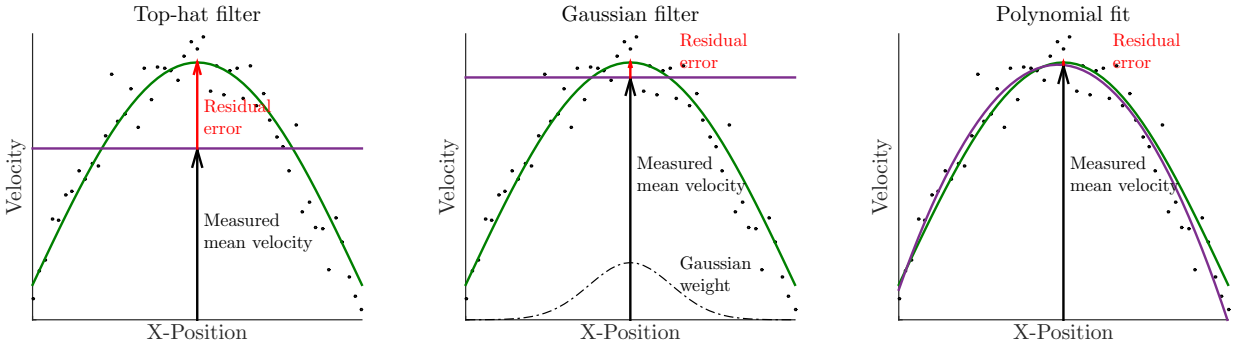

Figure 2: Illustration of sources of error due to residual velocity gradient within an interrogation spot. (•) Particles velocities; (—) Exact mean field; (—) Filtered mean field.

2.3. Reducing the error due to unresolved velocity gradient

Apart from the frustration of being limited in spatial resolution, a large final interrogation spot has a detrimental effect on the evaluation of the velocity statistical moments. The effect of the impulsive response of the interrogation algorithm on the statistics is a widely explored topic in the field of PIV. Saikrishnan et al (2006) compared Dual-Plane PIV data with DNS simulations in the logarithmic region of a turbulent boundary layer, and demonstrated that PIV is a suitable tool for statistics extraction provided that the small scales are sufficiently resolved (in their experiments a final interrogation spot of 24.6x24.6 wall units was sufficient). Lavoie et al (2007) investigated the modulation effects of PIV due to spatial averaging in decaying homogeneous isotropic turbulence, and proposed a correction based on previous knowledge of the velocity spectra. Atkinson et al (2014) studied the 3D spatial filtering and noise effects in terms of resolution on the Reynolds stresses and velocity power spectra. They demonstrated that the limited spatial resolution can easily lead to strong underestimation of the Reynolds stresses (up to 50% in their application to wall turbulence), but measurement noise can offset this effect, thus leading to ambiguity in determining the uncertainty on the measurement of turbulent statistics. Notwithstanding the large interest on the modulation effects in standard PIV, the extension of these considerations to ensemble PTV is still an unexplored field. In the following a discussion on the consequences of a poorly resolved mean velocity field on the estimation of Reynolds stresses is reported, as well as two possible solutions to reduce its effects.

In Figure 2, the source of error coming from assuming constant velocity within the interrogation spot is made evident by supposing the problem to be 1D for illustration purposes. Consider the particle local velocities spread around the mean velocity profile within one interrogation spot and the mean being variable due to an unresolved velocity gradient. In the standard ensemble PTV approach, all velocity vectors would have the same weight, thus resulting in a top-hat filtered mean velocity field (Figure 2, left). More importantly, second order moments would be computed around a mean value supposed

to be uniform in space within the interrogation spot, which would result in a spurious contribution to the turbulent kinetic energy.

In this work, we propose two approaches to tackle this problem. The first approach consists in weighting the velocity contributions to the statistical moments according to their distance with respect to the center of the interrogation spot. For example, by applying a Gaussian weighting function, the error in the central part is reduced according to the improved spectral response of the algorithm. Second order moments are still affected by large errors, but due to the improved mean velocity measurement in the central part of the window, the regions with larger deviations are those with lower weight, thus reducing their spurious contribution. Obviously, the price to pay is a larger number of particles to reach convergence; however, this is not exactly equivalent to use a smaller window with a top-hat approach, since peripheral particles are still participating in building up the signal, even though with smaller weights.

The second approach is that of enjoying the large amount of particles within the window to fit the distributions with a polynomial function. In this work, we used a second order polynomial function in x, y and z so that, for each particle n in the averaging region, each of its associated velocity components is expressed as a second order polynomial which is a function of the distance $(\Delta x_n, \Delta y_n, \Delta z_n)$ to the grid point considered. For instance, the velocity component u for particle n can be modelled as in Eq. 8. When doing this for the N_p particles contained in the interrogation volume, a system of equations is obtained, where the unknowns are the coefficients of the polynomial fit, $a_0, a_1, \ldots a_9$.

$$\begin{aligned} u_n = a_0 + a_1\Delta x_n + a_2\Delta y_n + a_3\Delta z_n + a_4\Delta x_n^2 + a_5\Delta x_n\Delta y_n \\ + a_6\Delta y_n^2 + a_7\Delta x_n\Delta z_n + a_8\Delta y_n\Delta z_n + a_9\Delta z_n^2 \end{aligned} \tag{8}$$

Expressing the system of equations in matrix form, we can solve for the the vector of coefficients, $\overline{a}$, arriving at Eq. 9, where $\overline{u}$ is the vector of particles' velocities and $\overline{\overline{M}}$ is the matrix that completes the system.

$$\overline{a} = (\overline{\overline{M}}^T\overline{\overline{M}})^{-1}\overline{\overline{M}}^T\overline{u} \tag{9}$$

Then, the value of the polynomial fit at the center of the window determines the corresponding component of the mean velocity vector associated to that interrogation spot. The advantage of this approach is that second order moments are computed with respect to a locally adapted mean, thus improving precision. Additionally, all particles are used with the same weight, thus removing the detrimental effect of the weighting windows of reducing the effective density. From now on, this method will be referred to as polynomial fit. It is important to remark that the polynomial approach is still a spatial averaging over the interrogation domain, even though "weighted" in a non-linear way. This has two important consequences. The first one is that non-uniformity of the fluctuations intensity distributions within the window cannot be accounted for, as a single value of the Reynolds stresses per window is delivered. The second is that the method essentially delivers a sort of weighted spatial average of the statistical moment.

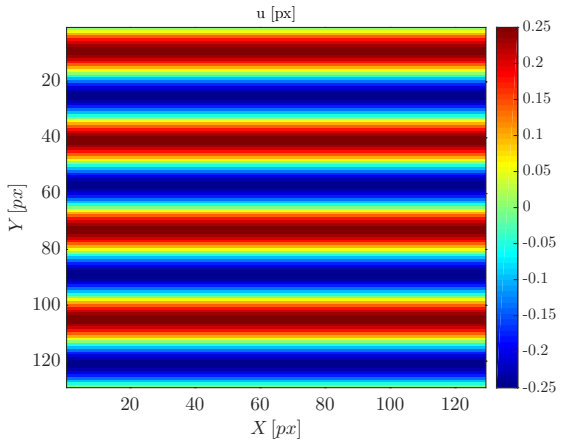

Figure 3: Mean sinusoidal field $\bar{u}$ used in the 2D test case for algorithm validation.

3. Validation

3.1. 2D test case

The performances of the proposed methods are tested on 2D images with imposed sinusoidal displacement. The 2D algorithm is different from the one sketched in Figure 1 only for the step 2, in which particles are simply identified with Gaussian interpolation on the images. A set of 200 image pairs is generated, with particle image density of 0.01 ppp, thus resulting in approximately 10 particles in a 32×32 pixels interrogation spot for PIV, and size of 128×128 pixels. The particle image diameter is set to 3 pixels. The simulated displacement field is depicted in Figure 3 and can be described as:

$$u_{exact} = 0.25 sin\left(2\pi \frac{y}{\lambda}\right) \tag{10}$$

with λ being the wavelength of the displacement and y being the vertical coordinate in the images.

The sinusoidal test allows to quantify the Modulation Transfer Function (MTF) of the algorithm, thus giving a straightforward evaluation of the spatial resolution. The MTF is calculated from a least-squares fitting of the measured displacement to a sinusoidal function. It can be demonstrated that this leads to:

$$MTF = \frac{\sum_{i=1}^{n} u_i u_{exact}}{\sum_{i=1}^{n} {u_{exact}}^2} \tag{11}$$

being n the number of grid points and u_i the measured mean displacement.

In Figure 4, the performances of standard PIV –performed with a classical top-hat correlation algorithm with interrogation spot of 32×32 pixels– and of the ensemble PTV with Top-hat and Gaussian filters and polynomial fit are presented. The ensemble PTV methods are applied on circular interrogation spots of 16 pixels of diameter, thus resulting on average in 400 particles for each interrogation spot. The results are reported in terms of the normalized frequency W/λ, where W is the interrogation window size for

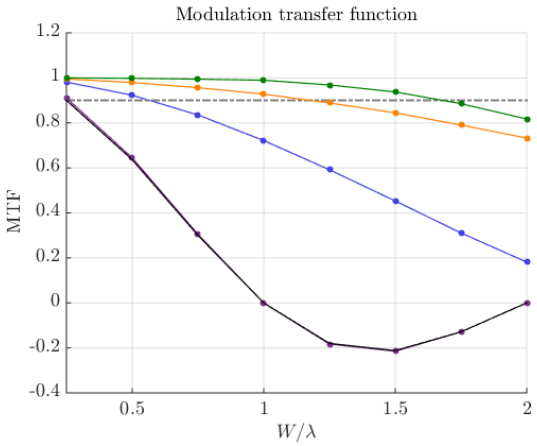

Figure 4: Modulation Transfer Function as a function of the normalized frequency. (—) Sinc function; (—) Top-hat filter; (—) Gaussian filter $\sigma = 1/4$; (—) Polynomial fit; (—) PIV. The line corresponding to MTF = 0.9 (- - -) is also depicted for reference.

the PIV process, namely $W = 32$ pixels in this case. The argument behind this choice is to set a comparison between what can be achieved with a standard PIV experiment (with the limit of the minimum number of 7-10 particles within the interrogation windows) and using the ensemble PTV process given the generated dataset. It is clear, nonetheless, that the ensemble PTV resolution can be pushed *ad libitum* increasing the number of samples. The comparison with PIV has to be interpreted only as indicative in this case.

The impulsive response of the PIV process, as expected, follows with good approximation $sinc(W/\lambda)$. As for the ensemble PTV with top-hat filter, the MTF is not exactly following a sinc since the displacement is 1D while the interrogation spots are circular. The adopted Gaussian filter has a standard deviation equal to 1/4 of the interrogation spots, and it allows to achieve a noticeable improvement of the MTF. However, the polynomial fit achieves strikingly high MTF, even higher than 0.8 at $\lambda = D_I = 16$ pixels. If a cut-off wavelength is estimated by considering the wavelength in which MTF falls below 0.9 (depicted in grey in Figure 4 for illustration purposes), the cut-off is set at $\lambda_{cut-off} = 3.8W$ for standard PIV, $\lambda_{cut-off} = 1.8W$ for ensemble PTV with top-hat average, $\lambda_{cut-off} = 0.8W$ for ensemble PTV with Gaussian averaging and $\lambda_{cut-off} = 0.6W$ for the case of the polynomial fit.

Thus, we can conclude that the polynomial fit is approximately equivalent to working with a 3 times smaller interrogation window than the top-hat moving average, but still maintaining the same number of particles. In other words, it reduces potentially by 3^N times (with $N = 2$ for 2D measurements and $N = 3$ for 3D measurements) the number of samples required to reach the same accuracy and resolution on the mean displacement.

An additional test case has been performed in which random noise has been superimposed on a mean sinusoidal displacement described by Eq. 10 with $\lambda = 32$ pixels. The random noise has a maximum intensity of 0.25 pixels^2, and it is sinusoidally

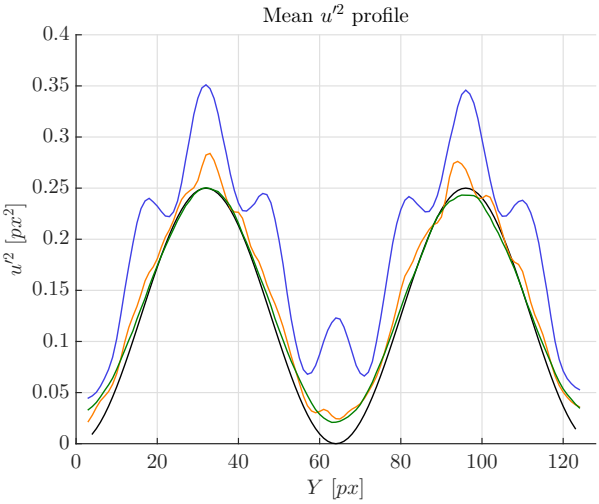

Figure 5: Mean profile of the squared velocity fluctuations (—) Exact solution; (—) Top-hat filter; (—) Gaussian filter $\sigma = 1/4$; (—) Polynomial fit.

distributed along the y direction similarly to the mean sinusoidal field but with a different wavelength, namely $\lambda_{u'} = 128$ pixels. Note that, in absence of an unresolved mean displacement, the three presented methods for ensemble PTV are equivalent.

The results reported in Figure 5 show that the mean streamwise square turbulence fluctuations profile (averaged over 128 x-lines) is contaminated by the unresolved mean sinusoidal displacement. This effect is much less pronounced on the ensemble PTV with Gaussian filter, even though the detrimental effect of reducing the number of particles affects the convergence of the results. The profile obtained with ensemble PTV when using the polynomial fit follows with quite good fidelity the exact profile, observing some discrepancy at low turbulence intensity due to the smoothing effect of the window size and the residual error in the particles identification step. The contour maps for this same magnitude, u'^2, are presented in Figure 6, where the modulation errors of the top hat filter and the convergence issues of the gaussian filter can be easily observed.

3.2. 3D test case

The algorithms are validated with a 3D synthetic test using four cameras imaging a $10 \times 10 \times 10\,\mathrm{mm}^3$ with a resolution of 20 pixels/mm. The cameras form a square, with each camera forming an angle of approximately 35 degrees both in pitch and yaw. The volume is seeded with 400 particles, thus resulting in a particle image density of 0.01 ppp and in a volumetric concentration of $5 \cdot 10^{-5}$ ppv (particles per voxel), assuming that a resolution ratio of 1 between voxels and pixels is used for reference. The particle image diameter is about 3 pixels. A set of 2000 volume pairs, each reconstructed from the four 2D views, is generated to perform ensemble averaging. A jet-like displacement flow field with a pseudo-shear layer with random turbulence was simulated. The jet is directed along the x direction of the volume, and it has an axisymmetric cosinusoidal profile, as

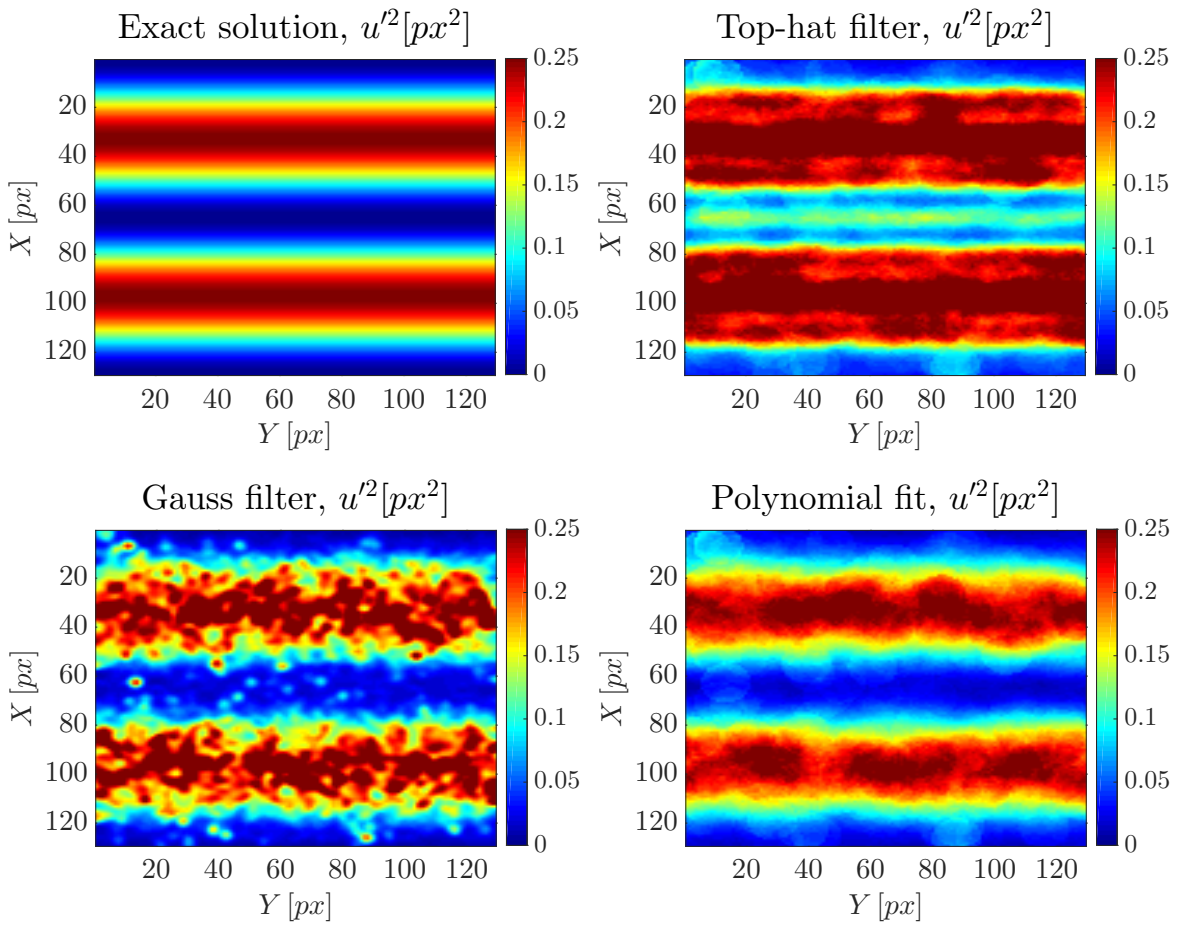

Figure 6: Contour maps of the squared velocity fluctuations: comparison between the exact solution and the results obtained with the top-hat, gaussian filters and the polynomial fit.

described in Eq. 12:

$$u = 1.5\left[1 + cos\left(2\pi\frac{r}{\lambda}\right)\right] \tag{12}$$

with r being the radial distance from the x axis. The maximum displacement is set to 3 voxels, while the wavelength λ increases linearly with the x coordinate, ranging between 60 and 90 voxels. A pseudo-turbulence is generated by adding random noise on the local velocity in a shear layer centered at $r = 0.5\lambda$ and with thickness of 0.4λ (thus ranging between 24 and 36 voxels). A degree of correlation is added between axial and radial fluctuations, while tangential fluctuations are statistically uncorrelated either with the axial or the with radial ones. Spherical interrogations spots with diameter of 16 voxels are used for ensemble PTV, thus resulting in about 200 particles for each interrogation spot according to Eq. 5. Besides, an additional set of 500 volume pairs with particle image density of 0.05 ppp has been generated to perform an equivalent Tomographic PIV experiment under the same flow field conditions. The interrogation spot chosen for Tomo PIV is $40 \times 40 \times 40$ voxels, containing in average 16 particles.

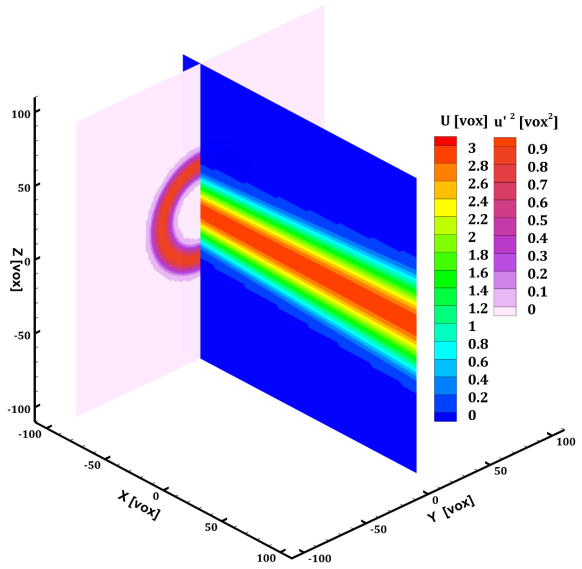

Figure 7: Exact velocity field: $Y = 0$ plane contoured with mean streamwise velocity component; $X = -5mm$ plane contoured with the intensity of the squared streamwise velocity fluctuations.

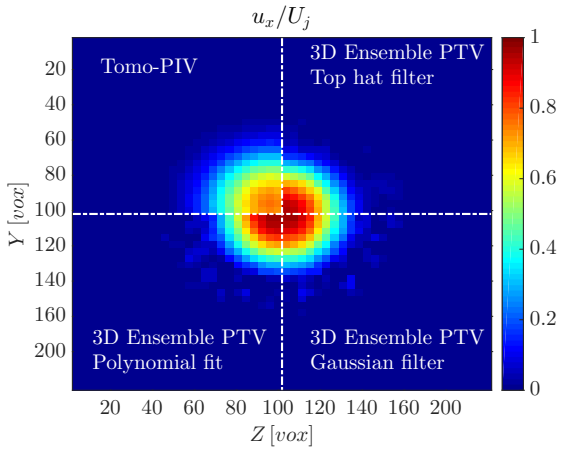

Figure 8: Comparison of the mean streamwise velocity component in the $X = -5mm$ plane: tomographic PIV vs. ensemble averaging PTV with different filtering approaches.

The exact velocity field is represented in Figure 7, while the test results are presented in non-dimensional form in cylindrical coordinates in the Figures 8 and 9 in terms of mean velocity and turbulence fluctuations. The symbols u'_x, u'_r and u'_ϑ indicate respectively the fluctuations in the axial, radial and tangential directions. The maps reported in the Figures 8 and 9 have to be intended as ensemble averages. It is important to note that the simulated turbulence lacks instantaneous spatial coherence and therefore it is not possible to assess the performance of tomographic PIV on the turbulent fluctuations.

The smoothing effect due to the larger interrogation spot size is evident on the

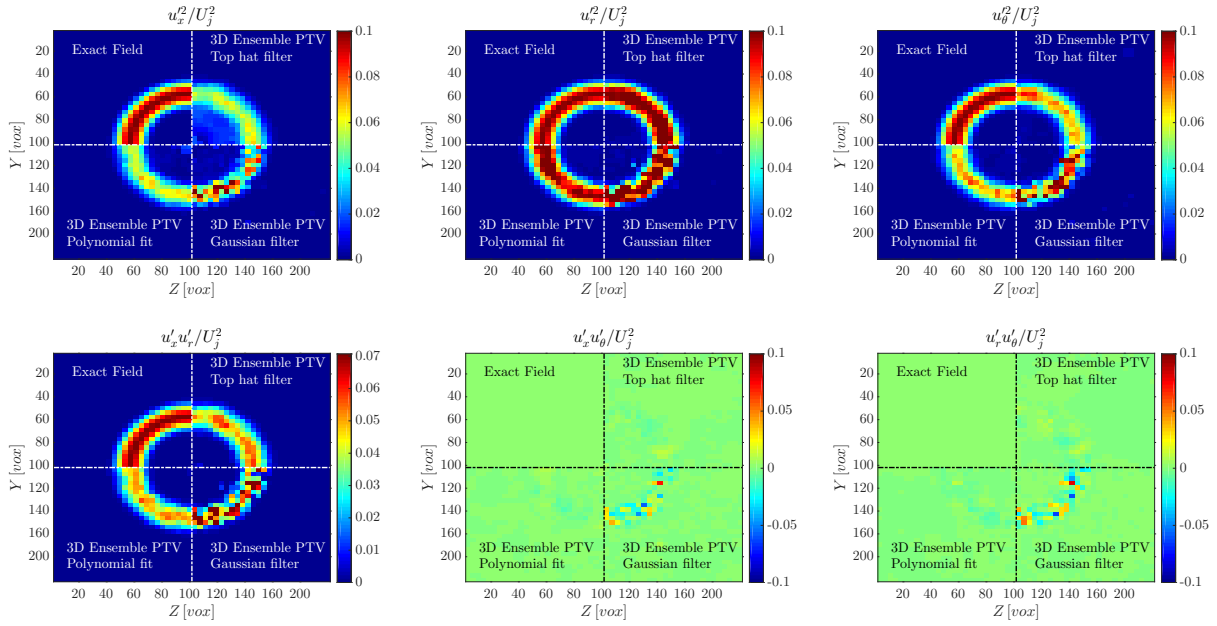

Figure 9: Turbulent fluctuations in the $X = -5mm$ plane using Ensemble PTV with the top-hat, and gaussian filters as well as the polynomial fit and comparison with the exact solution.

tomographic PIV mean flow field (Figure 8). The ensemble PTV filters seem to provide very similar results, even though a data inspection reveals a slightly higher modulation of the velocity peak on the jet axis with the top hat filter, coherently with the results of the previous section. An evidence of this is the contamination in the region close to the jet axis of the intensity of the axial turbulent fluctuations achieved by ensemble PTV with a top hat filtering, as it can be seen in Figure 9, top-left. The data obtained with the polynomial fit and the Gaussian filter seem to be much less affected by this issue. However, the intensity of the turbulent fluctuations calculated with the Gaussian filter is significantly contaminated by noise, thus showing poor convergence. In fact, this problem is clearly observed in all the turbulent fluctuations results in Figure 9 and is due to the effective lower number of particles used within the averaging process, as discussed in the previous section.

4. Experimental validation

The experimental validation of the technique is performed on a turbulent round jet flow. The experiments are carried out in the water jet facility at the University of Naples Federico II schematically represented in Figure 10. A round jet is issued through a short pipe nozzle (diameter D = 20 mm and length 6.2D) mounted on the bottom wall of a nine-sided Plexiglas water tank facility, as the one used in Cafiero et al (2014). A centrifugal pump is used to feed the circuit with the required mass flow rate of about 0.5 kg/s, corresponding to a Reynolds number based on the nozzle diameter D

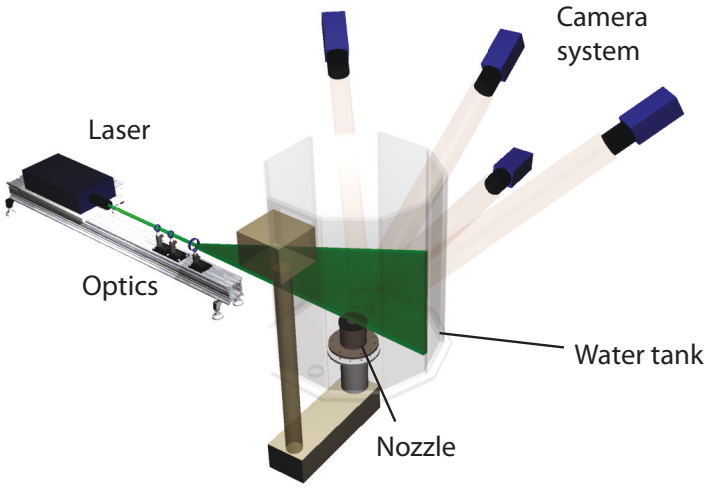

Figure 10: Schematic representation of the water jet facility.

equal to about Re =30, 000. The working fluid passes through a stagnation chamber (diameter $5D$ and length $20D$), where two sets of grids are introduced in order to remove fluctuations due to the feeding circuit. The water is then forced within the short pipe nozzle, which discharges within the water tank.

The flow is seeded with neutrally-buoyant polyamide particles (mean diameter equal to $56\,\mu$m) uniformly dispersed within the tank. The seeding density depends upon the experiment: for the Tomographic PIV a standard particle image density of 0.05 ppp is used, whilst for the Ensemble PTV experiment a much lower density is employed, of the order of $0.003 - 0.005$ppp.

The investigated area is illuminated from the side using a Quantel Evergreen Nd:YAG Laser for PIV applications (200 mJ/pulse, 15 Hz). For both the Tomo-PIV and the Ensemble PTV experiments the laser beam is shaped into a rectangular cross section volume by means of a lenses system. Moreover, the exact volume thickness is adjusted introducing a knife-edged mask, which sets it to $1.5D$. The imaging system is composed of four Andor sCMOS Zyla 5.5 Mpixels equipped with Tokina objectives (100 mm focal length, $f_{\#} = 16$); three of them are disposed in Scheimpflug arrangement, whilst one faces directly the illuminated region. The imaged region extends for about $5D$ in the streamwise direction (Y) and $5D$ in the crosswise direction (X); it is discretized with a digital resolution of about 10 voxels/mm.

An optical calibration procedure is performed by recording images of a target (black dots on white background, 5 mm pitch) translated with micrometric precision through the measurement volume. The target images are captured in correspondence of seven equally spaced locations along the direction orthogonal to the target plane. The mapping function is obtained using the pinhole camera model, as suggested by Tsai (1987). The resulting maximum calibration error is of the order of 0.5 pixels. A self-calibration

procedure (Wieneke, 2008) is then carried out in order to further correct the location of the laser volume using the scattering particles and to reduce reciprocal misalignments of the cameras. This leads to a reduction of the calibration error down to 0.03 pixels.

A pre-processing is applied to the raw images in order to reduce the background noise and improve both tomographic reconstruction for Tomo-PIV and particle detection for the ensemble PTV. The pre-processing consists in the temporal minimum image subtraction, in order to limit the effect of laser reflections within the flow. Additionally, a sliding minimum subtraction (with window size of 7×7 pixels) has been performed to remove the residual fluctuating part of the background.

For the tomographic PIV experiments, the 3D volume is reconstructed from the pre-processed images using four C-SMART iterations on a binned volume (Discetti and Astarita, 2012b) three C-SMART iterations on the full volume, one MTE iteration (Novara et al, 2010) aimed to detect and remove the ghost particles generated during the reconstruction process, 3 further C-SMART iterations on the full volume and finally one SMART iteration. The resulting volume extends for $1000 \times 1000 \times 300$ voxels.

During the iterative reconstruction with C-SMART, a non-isotropic Gaussian smoothing is applied on a $[3 \times 3 \times 1]$ kernel (Spatial filtering improved tomography, Discetti et al, 2013) in order to reduce the artefacts of the reconstruction due to particles elongation along the depth direction in the reconstructed volumes. In order to check the quality of the reconstruction, the signal to noise ratio defined as the reconstructed particles intensity inside the illuminated region (true particles + ghost particles) versus that reconstructed outside (ghost particles) is calculated. The S/N ratio results to be larger than 2.5, which is a typical value for a good reconstruction (Scarano, 2013).

The reconstructed volumes are interrogated using an efficient 3D cross-correlation algorithm (Discetti and Astarita, 2012a) based on sparse correlations on blocks to reduce the amount of redundant operations when using overlapping windows. The final windows size is $48 \times 48 \times 48$ voxels, 75% overlap, thus leading to a vector pitch of 1.2 mm. A Blackman weighting window is used both on the correlation map and on the velocity to properly tune the spatial resolution and to ensure the stability of the PIV process.

The ensemble PTV process is applied on 49000 snaphots triangulating particles with a search radius on the images of 3 pixels. The low image density ensures that the number of ghost particles is less than 1%, according to Eq. 1 (Discetti and Astarita, 2014). In order to compensate for the large particles displacement (the jet bulk velocity corresponds to approximately 12 pixels for the chosen time separation between the exposures) and maintain a small search radius, a predictor mean field has been constructed using the low density snapshots captured for the ensemble PTV. The use of a predictor field to bias the particles search in PTV is a well assessed procedure (commonly referred as super-resolution PTV, Keane et al, 1995); in the presented case the additional difficulty is that the particles concentration is relatively low, thus affecting the cross-correlation signal strength. For this reason a pseudo-reconstructed volume pair has been built summing particles detected on the first and second exposure of 500

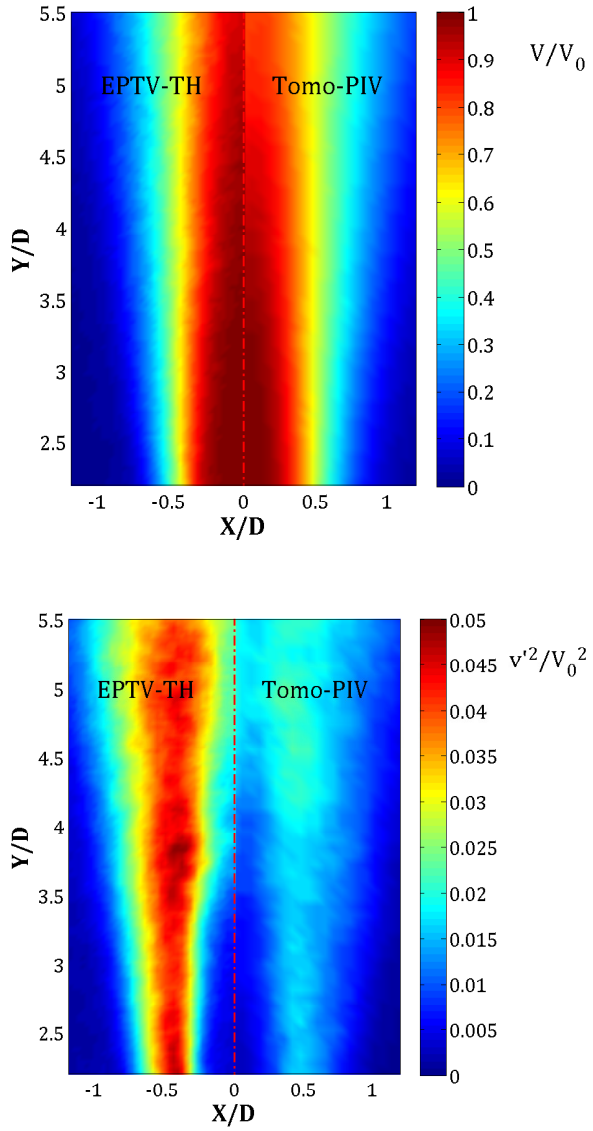

Figure 11: Comparison of the mean axial velocity and axial and radial velocity fluctuations on the plane $Z = 0$ for the case of Ensemble PTV with a top-hat approach and Tomo-PIV

snapshots. Gaussian blobs with diameter of 3 voxels at 10 voxels/mm resolution have been generated around the particles location. The volumes are cross-correlated with interrogation windows of 24^3 voxels, 50% overlap. Subsequently, a biased matching search using the calculated predictor and a search radius of 8 voxels has been carried out. Finally, the results are averaged over cubic blocks with 24 voxels side (thus leading to a resolution of 2.4 mm) and spacing of 6 voxels (i.e. 0.6 mm). It has to be remarked that for the mean velocity field much smaller averaging regions would already suffice for the task of an acceptable accuracy, considering that for the chosen resolution the average number of velocity vectors is of the order of 8000.

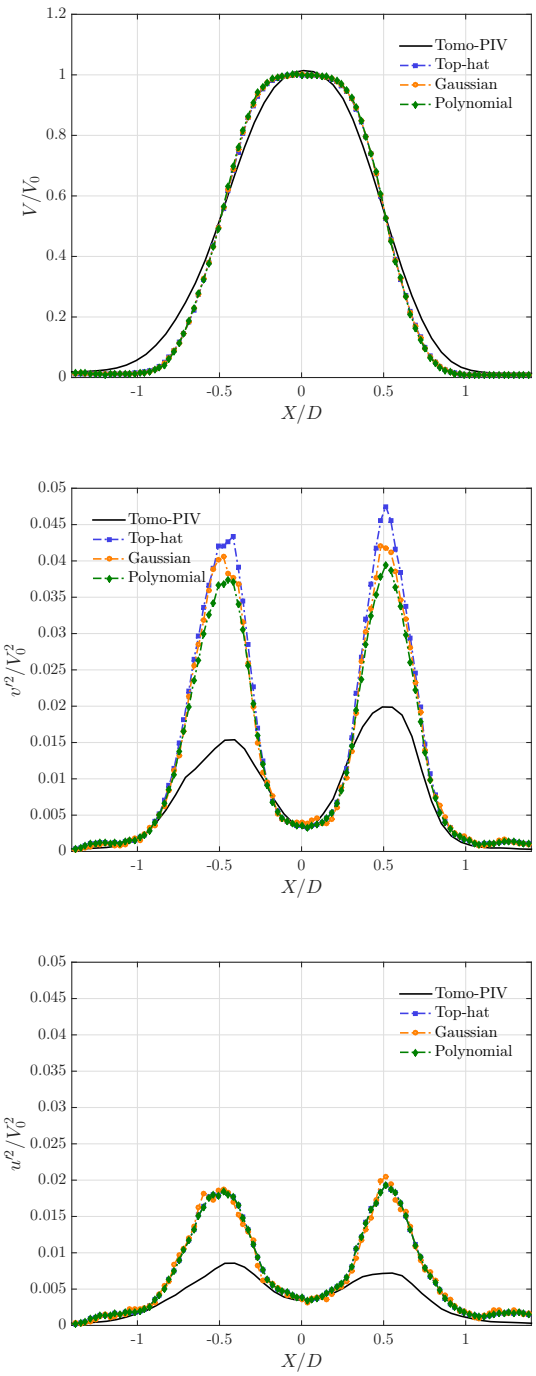

Figure 12: Comparison of the mean axial velocity and axial and radial velocity fluctuations obtained using the Tomo-PIV (continuous black line) and EPTV approach with the top-hat, gaussian and polynomial fit approaches

The results of Tomo-PIV and Ensemble PTV are compared in terms of mean streamwise velocity and intensity of the streamwise velocity fluctuations on the mid-plane of the jet in Figure 11. As foreseeable, Tomo-PIV provides a smeared velocity distribution, with a lower peak of average velocity on the jet axis and fictitiously larger

jet diameter if compared to the Ensemble PTV. This has to be addressed to the larger interrogation regions, as well as to the modulation effect of ghost particles motion. The effects of limited spatial resolution are similarly evident in the evaluation of the streamwise Reynolds stress distribution, with significantly underestimated values of the fluctuation intensity, as well as a wider measured shear layer.

The comparison of the mean axial velocity V/V_0, the squared axial and radial velocity fluctuation (v'^2/V_0^2 and u'^2/V_0^2, respectively) obtained using the Tomo-PIV and the Ensemble PTV is reported in Figure 12 in form of profiles. The profiles are extracted at $2.5D$ from the nozzle exit section. The three tested Ensemble PTV approaches achieve a much better resolution of the streamwise velocity profile than Tomo-PIV both due to a smaller averaging region and to the absence of ghost particles. Differences between the Ensemble PTV approaches are perceivable only in the region of high curvature of the streamwise velocity profile, where indeed modulation effects start being relevant. The unresolved part of the velocity profile is expected to show up on the Reynolds stresses. Indeed, the profiles of the streamwise normal Reynolds stress reported in Figure 12 show that the differences between the used algorithms are significant. While if compared to Tomo-PIV in all 3 cases the profile of v'^2 is closer to the physical representation of a relatively unperturbed potential core and of relatively thin shear layer turbulence production regions, remarkable differences are experienced on the peak intensity values. The top-hat approach, which is supposed to have lower spatial resolution, leads to the largest intensity value of the peak of v'^2/V_0^2. It can be inferred that the differences have to be addressed to poorer resolution of the mean field. The sharper peaks observed when using the top-hat approach can be ascribed, indeed, to the modulation effects of the mean velocity profiles, as they occur in the region of larger curvature of the mean field. A further evidence that the only reason for differences between the top hat and the polynomial method is the resolution of the mean velocity is given by the profiles of the radial velocity fluctuations intensity u'^2/V_0^2. Since the mean radial velocity is small and well resolved, there is no modulation effect observable, thus top-hat and polynomial approaches are practically equivalent. The Gaussian filter, coherently with what observed on the axial component, exhibits convergence issues due to the small equivalent number of particles. These results are perfectly in line with the contamination of computed Reynolds stresses distributions due to the poorly resolved mean velocity field outlined on the basis of theoretical arguments in Sec.2.3 and observed in Sec.3. It can be concluded that, provided that the mean velocity field is adequately resolved, the polynomial and top-hat approaches are practically equivalent, while the Gaussian filtering approach is more affected by convergence issues.

5. Conclusions

The performance of ensemble particle tracking velocimetry to extract high resolution three-dimensional turbulent statistics has been assessed. Owing to the low concentrations typical of volumetric experiments (both due to the introduction of the

third dimension and to the low particle image density to be set to limit the occurrence of ghost particles), two methods have been proposed to improve the computation of the mean velocity components and to reduce the contamination of second order moments due to unresolved velocity gradients. The first method, based on the use of weighting functions to modulate the impulsive response of the averaging window, is affected by an effective lower number of particles used within the averaging process due to the introduction of weights. The second method, based on fitting locally the velocity vectors distribution with a polynomial function and computing statistical moments around the locally adaptive fit, reduces significantly the modulation error, acting as a top-hat filtering with an approximately 3 times smaller window. This allows to reduce the number of required samples to achieve the same spatial resolution in 3D by a factor of $\sim 3^3$ times if compared to the standard 3D ensemble PTV process. The reported applications in the 3D scenario (both synthetic and experimental) show encouraging results in terms of potential improvement of the spatial resolution.

6. Acknowledgements

Stefano Discetti was partially supported by Grant TRA2013-41103-P of the Spanish Ministry of Economy and Competitiveness. This grant includes FEDER funding. Nereida Agüera was supported by the fellowship Beca de colaboración 2015/16 of the Spanish Ministry of Education.

References

Adrian RJ (1991) Particle-imaging techniques for experimental fluid mechanics. Annual review of fluid mechanics 23(1):261–304

Atkinson C, Buchmann NA, Amili O, Soria J (2014) On the appropriate filtering of piv measurements of turbulent shear flows. Experiments in fluids 55(1):1–15

Avallone F, Discetti S, Astarita T, Cardone G (2015) Convergence enhancement of single-pixel PIV with symmetric double correlation. Experiments in Fluids 56(4):1–11

Cafiero G, Ceglia G, Discetti S, Ianiro A, Astarita T, Cardone G (2014) On the three-dimensional precessing jet flow past a sudden expansion. Experiments in fluids 55(2):1–13

Discetti S (2013) Tomographic Particle Image Velocimetry-Developments and applications to turbulent flows. PhD thesis, Università degli Studi di Napoli Federico II

Discetti S, Astarita T (2012a) Fast 3D PIV with direct sparse cross-correlations. Experiments in fluids 53(5):1437–1451

Discetti S, Astarita T (2012b) A fast multi-resolution approach to tomographic PIV. Experiments in fluids 52(3):765–777

Discetti S, Astarita T (2014) The detrimental effect of increasing the number of cameras on self-calibration for Tomographic PIV. Measurement Science and Technology 25(8):084,001

Discetti S, Natale A, Astarita T (2013) Spatial filtering improved Tomographic PIV. Experiments in fluids 54(4):1–13

Elsinga G, Westerweel J, Scarano F, Novara M (2011) On the velocity of ghost particles and the bias errors in Tomographic-PIV. Experiments in fluids 50(4):825–838

Elsinga GE, Scarano F, Wieneke B, van Oudheusden BW (2006) Tomographic particle image velocimetry. Experiments in fluids 41(6):933–947

Kähler CJ, Scharnowski S, Cierpka C (2012) On the resolution limit of digital particle image velocimetry. Experiments in fluids 52(6):1629–1639

Keane R, Adrian R, Zhang Y (1995) Super-resolution particle imaging velocimetry. Measurement Science and Technology 6(6):754

Lavoie P, Avallone G, De Gregorio F, Romano GP, Antonia R (2007) Spatial resolution of piv for the measurement of turbulence. Experiments in Fluids 43(1):39–51

Lynch K, Scarano F (2015) An efficient and accurate approach to MTE-MART for time-resolved Tomographic PIV. Experiments in Fluids 56(3):1–16

Maas H, Gruen A, Papantoniou D (1993) Particle tracking velocimetry in three-dimensional flows. Experiments in Fluids 15(2):133–146

Nobach H, Honkanen M (2005) Two-dimensional gaussian regression for sub-pixel displacement estimation in particle image velocimetry or particle position estimation in particle tracking velocimetry. Experiments in fluids 38(4):511–515

Novara M, Batenburg KJ, Scarano F (2010) Motion tracking-enhanced mart for tomographic PIV. Measurement science and technology 21(3):035,401

Saikrishnan N, Marusic I, Longmire EK (2006) Assessment of dual plane piv measurements in wall turbulence using dns data. Experiments in fluids 41(2):265–278

Scarano F (2013) Tomographic PIV: principles and practice. Measurement Science and Technology 24(1):012,001

Scharnowski S, Hain R, Kähler CJ (2012) Reynolds stress estimation up to single-pixel resolution using PIV-measurements. Experiments in fluids 52(4):985–1002

Soria J, Willert C (2012) On measuring the joint probability density function of three-dimensional velocity components in turbulent flows. Measurement Science and Technology 23(6):065,301

Tsai RY (1987) A versatile camera calibration technique for high-accuracy 3d machine vision metrology using off-the-shelf TV cameras and lenses. Robotics and Automation, IEEE Journal of 3(4):323–344

Westerweel J, Geelhoed P, Lindken R (2004) Single-pixel resolution ensemble correlation for micro-PIV applications. Experiments in Fluids 37(3):375–384

Wieneke B (2008) Volume self-calibration for 3d particle image velocimetry. Experiments in fluids 45(4):549–556

Wieneke B (2013) Iterative reconstruction of volumetric particle distribution. Measurement Science and Technology 24(2):024,008